Available online at www.sciencedirect.com
SCIENCE DIRECT®
Nuclear Instruments and Methods in Physics Research A 535 (2004) 1–15
NUCLEAR INSTRUMENTS & METHODS IN PHYSICS RESEARCH Section A
www.elsevier.com/locate/nima

Trends and new developments in gaseous detectors

M. Hoch*

CERN, Geneva 23, Switzerland

Available online 27 August 2004

Abstract

Almost one century ago the method of particle detection with gaseous detectors was invented. Since then they have been exploited successfully in many experiments using a wide variety of different applications. The development is still going on today. The underlying working principles are today well understood and with the help of modern simulation techniques, new configurations can be easily examined and optimized before a first experimental test.

Traditional wire chamber ensembles demonstrate that they are still up to date and are well prepared to meet also the challenges of LHC. Applications will be discussed using TPCs in high multiplicity environments with standard Multi-Wire Proportional Chamber (MWPC) as readout as well as drift tubes in a muon spectrometer for a Large Hardron Collider (LHC) experiment. Triggered by the evolving printed circuit technology, a new generation of gaseous detectors with very high position resolution and rate capability has emerged. Two representatives (MICROMEGAS, GEM) have proved their reliability in various experiments and are promising candidates for future projects. Performance and results will be discussed for these detectors. Furthermore, achievements in RPC-based detectors will be discussed. The standard Trigger RPC is a reliable low-cost semi-industrial manufactured device with good time resolution. Thin gap RPCs (Multigap-, and High Rate Timing RPC) show very fast signal response at high efficiency and significantly increased rate capability and will be applied in TOF detectors.

Keywords: Gaseous detectors

1. Introduction

The working field of gaseous detectors began almost one century ago, when H. Geiger E. Rutherford and W. Mueller started to use their knowledge in gas discharges to build a device to detect charged particles, known as the Geiger-Mueller counter [1,2]. The proportional counter and later the Multi-Wire Proportional Chamber (MWPC) [3] opened the door to a wide range of applications, which are still being used and optimized. Modern etching technology initiated a boom of micro structure devices, now known as Micro-Pattern Gaseous Detectors (MPGD). The Gas Electron Multiplier (GEM) [4] and the MICRO

*Tel.: +0041-22-767-8434; fax: 0041-22-767-3200.
E-mail address: michael.hoch@cern.ch (M. Hoch).

0168-9002/$ - see front matter © 2004 Elsevier B.V. All rights reserved.
doi:10.1016/j.nima.2004.07.265

MEsh GAseous Structure (MICROMEGAS) [5] are two of their representatives, used successfully in different experiments. An advance in the domain of Parallel Plate Counters (PPC) is represented by the Resistive Plate Chamber (RPC) [6], which combines fast signal response with good rate capability.

In the past nearly all High Energy Physics experiments successfully used gaseous detectors, exploring their features, like good spatial resolution, big and fast signals, good energy deposition per unit length (dE/dx), low radiation length, etc. Their performance and adaptability to the needs of the experiments make them still indispensable today. Good examples are the numerous and diverse gaseous detectors employed in the Large Hardron Collider (LHC) experiments, being assembled right now. However, the large number of highly interesting contributions to this conference impressively demonstrate that the interest of researchers in the field of gaseous detectors are far from being exhausted. Efficient detector development requires precise and highly reliable simulation tools. Listed below are some of the 'state of the art' simulation tools: MAXWELL [7] allows to calculate two-dimensional (2D) and three-dimensional (3D) field maps for arbitrary electrodes and dielectrics. With HEED [8], the energy loss and the ionization processes can be simulated. MAGBOLZ [9] is mostly used for electron transport properties such as drift and diffusion, and also multiplication and attachment processes. With GARFIELD [10], one can compute equipotentials and can interface with the programs mentioned above. An analytical approach with MATHEMATICA [11] was presented at the conference [12]. And finally, PSPICE [13] is one of the programs commonly used for the signal processing of the electronic circuit.

2. Traditional wire chamber

Many different types of wire chambers have been developed in the past for a multitude of applications. I would like to discuss two examples of traditional wire chambers, which are well known in its basic principles, but nevertheless, modern and contemporary in todays implementation.

2.1. TPCs with MWPC readout at the STAR and ALICE experiment

The Time Projecting Chamber (TPC), invented in the 70s [14], is a simple but very effective detector allowing to trace particles in a volume, measure their momenta, and perform particle identification [15]. A TPC is a large volume filled with counting gas, with an electric field applied across it. On the end plate of the volume, readout chambers are installed. Charged particles traversing the chamber liberate electrons along their tracks. These electrons follow the electric field lines to the readout chambers where a signal is generated. From the 2D image of the tracks on the end plate, the third dimension can be calculated from the time the electrons need to arrive at the readout chambers. Thus, the TPC provides along the particle tracks many 3D space points. To measure the momenta of the particles a magnetic field is applied. The magnetic field is aligned parallel to the electric field, thus gas diffusion processes are reduced. The particle identification is performed by measuring the ionization loss of the traversing particle in the gas volume.

The STAR TPC: The Solenoidal Tracker At RHIC (STAR) experiment [16] is installed at the Relativistic Heavy-Ion Collider [17] located at the Brookhaven National Laboratory. Central collisions with a maximum center of mass energy for Au–Au $\sqrt{S_{NN}} = 200\,\text{GeV}$ per nucleon create typically 2000 tracks/event inside the acceptance of the central tracking device of a TPC. The cylindrical STAR TPC allows handling large multiplicity events, as shown in Fig. 1.

The outer cylinder of the STAR TPC has a length of 4.2 m and a diameter of 4 m. The signal readout is performed by MWPCs with cathode pads mounted on both end plates. A photo of such a readout chamber is shown Fig. 2. The pad shape is optimized to achieve the optimal position resolution. The chamber is divided into two sectors of pad size. The inner sector has pads with an area of $2.85 \times 11.5\,\text{mm}^2$, while at the outer sector

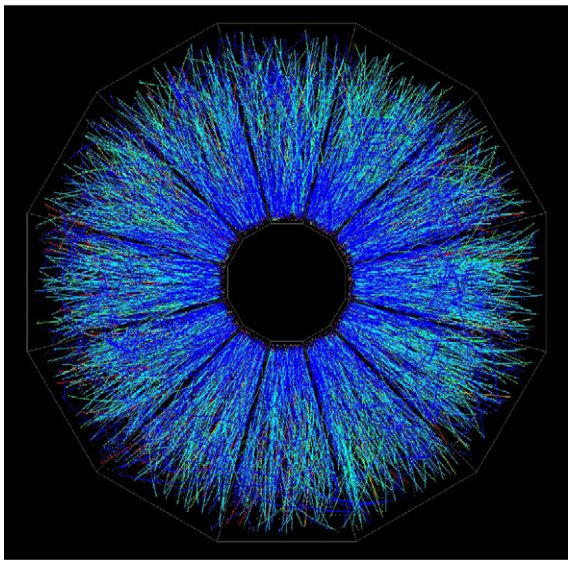

Fig. 1. STAR TPC event display.

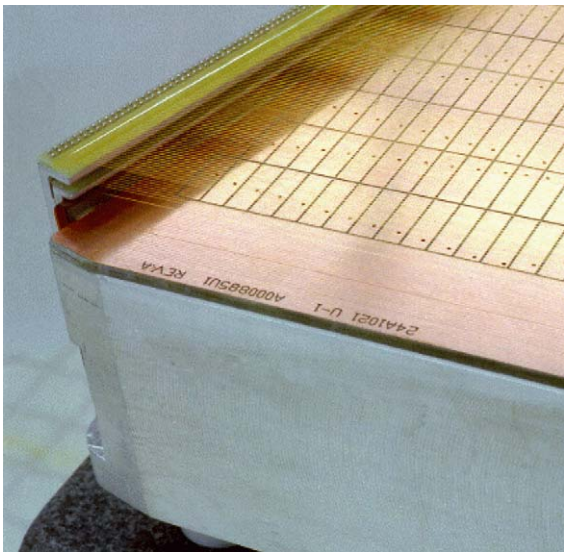

Fig. 2. TPC read out chamber.

$6.2 \times 19.5\,\mathrm{mm}^2$ to comply with the different occupancies. The STAR TPC has in total 136 608 readout channels. Due to the pad-response-function a $r-\phi$ resolution of $\sim$500 μm can be achieved.

At the STAR TPC [18], particles are identified over a momentum range from 100 MeV/c to >1 GeV/c and momenta are measured up to 30 GeV/c. The applied electric field of 135 V/cm is parallel to a homogeneous magnetic field of 0.5 T to measure the momenta of the traversing particle. The achieved $\mathrm{d}E/\mathrm{d}x$ resolution at the STAR TPC is 7%. In Fig. 3 the energy loss for particles traversing the TPC as a function of their momenta are plotted.

The ALICE TPC: A Large Ion Collider Experiment (ALICE) [19] is one of four experiments to be installed in the LHC. The main goal of ALICE, dedicated for heavy ion physics, is to obtain a fundamental understanding of the microscopic structure in hadronic interaction, at high densities and temperatures and study the signature of a possible Quark-Gluon Plasma. The LHC is designed as a proton–proton collider, but will have also a 1month/year period of Pb ion run. For central Pb–Pb collision, with a center of mass energy of $\sqrt{S_{\mathrm{NN}}} = 7.5$ TeV/nucleon, 2000–8000 charged particles per rapidity unit are expected. Thus the maximal expected multiplicity of $\mathrm{d}N_{\mathrm{ch}}/\mathrm{d}y < 8000$ will create up to 20 000 charged primaries and secondary tracks in the TPC acceptance. The ALICE TPC [20] is the central tracking detector in the experiment. To cover the acceptance of $|\eta| < 0.9$, the TPC has a double cylindrical design with an inner and outer diameter of 160 and 560 cm, respectively, and a total length of 510 cm.

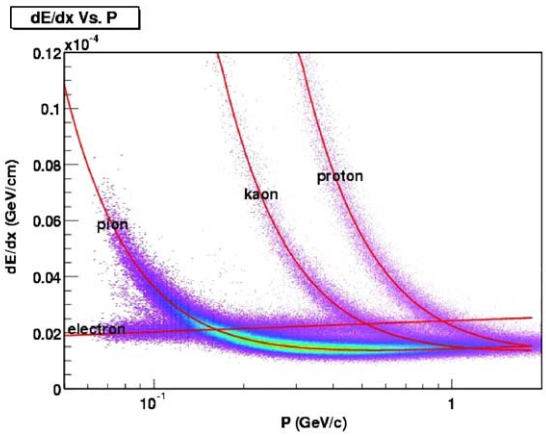

Fig. 3. STAR TPC energy loss distribution for primary and secondary particles as a function of p_{T} in the presence of a magnetic field of 0.25 T.

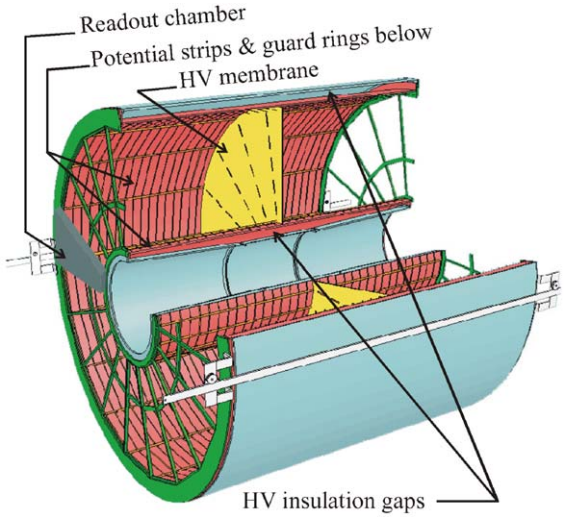

Fig. 4. TPC field cage.

A schematic of the TPC is shown in Fig. 4. To achieve the required momentum resolution of $<2\%$ at $1\,\mathrm{GeV}/c$ and $\sim 10\%$ at $10\,\mathrm{GeV}/c$ a magnetic field up to 0.5 T will be provided. For particle identification, the TPC is designed to achieve a $\mathrm{d}E/\mathrm{d}x$ resolution of $<7\%$ in the high-multiplicity environment of Pb–Pb collisions.

MWPC chambers with cathode-pad-readout will be installed on the two end caps of the TPC cylinder. The overall design is chosen to optimize for momentum and $\mathrm{d}E/\mathrm{d}x$ resolution, providing full azimuthal coverage. The radial dependence of the track density leads to changing requirements for the readout chamber design as a function of radius. Consequently, the readout plane is radial segmented into three zones with following pad shapes: inner most ($4 \times 7.5\,\mathrm{mm}^2$), middle ($6 \times 10\,\mathrm{mm}^2$) and outer ($6 \times 15\,\mathrm{mm}^2$). This design allows to achieve a space-point resolution $\sigma(r\phi) = 300\,\mu\mathrm{m}$ and $\sigma(z) = 600\,\mu\mathrm{m}$, as well as a two-track separation of 5 mm. Overall 570 132 pads cover both readout planes. Up to an occupancy of 50% at the innermost pad row and still 20% at the outer pads is expected.

To fulfill ALICE Physics requirements, such as minimal multiple-scattering and low secondary-particle production, the material budget has to be kept as low as possible.

Therefore, modern materials were adopted for the field cage construction, as well as the use of a light counting gas Ne/CO2 90/10% [21]. The field cage cylinders are made up of composite material, NOMEX honeycombs sandwiched in glass fiber. The overall radiation length of the TPC is $X_0 = \sim 3\%$. The field defining central electrode is a 25 μm aluminized Mylar foil, stretched over $32\,\mathrm{m}^2$ and glued on Al-rings. Due to the choice of the gas mixture, the TPC field cage has to operate with an electric field of 400 V/cm. To generate this field over the total drift length of 2500 mm, 100 kV has to be applied on the central electrode. Since the radial field components in the drift field would change the trajectory of the electrons, the sensitive volume is well defined by potential strips. These aluminized Mylar strips have a pitch of 15 mm and are detached from the cylinder surface, following the design of the NA49 experiment at CERN [22]. To get their correct potentials, the strips are supplied by a resistor chain. Fig. 5 shows a picture of the ALICE TPC drift volume. The mechanical structure and field defining network of the TPC are designed to keep radial field non-uniformities to $<10^{-4}$.

2.2. Drift tubes used for muon spectrometers

One example of an economical high-precision solution for large detection areas is the use of drift

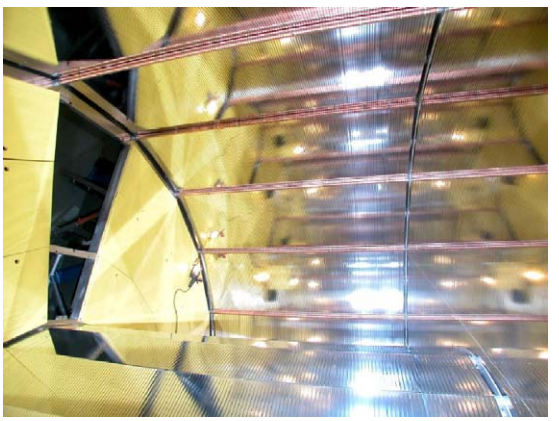

Fig. 5. Photo of the ALICE TPC drift volume, an open sector for the readout chamber, inner and outer cylinders covered with aluminized Mylar strips held by metalized polycarbonate rods.

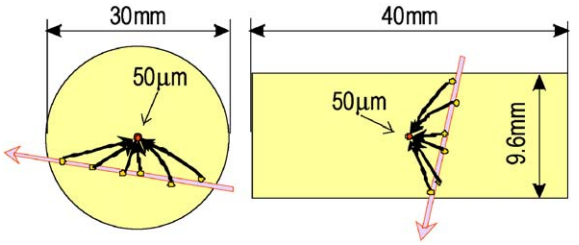

Fig. 6. Cross-section of the ATLAS (left) and CMS (right) muon spectrometer drift tubes.

tubes for a muon spectrometer. Two LHC experiments, ATLAS and CMS, are using a drift tube assembly for their muon spectrometer to identify and reconstruct muon tracks, measure their momentum, and provide matching information to the inner detector system. A cross-section of the chamber designs for ATLAS and CMS is shown in Fig. 6 [23,24]. The basic detection element of the ATLAS MDT chambers is a 30 mm diameter aluminum drift tube with 400 μm thick walls and a 50 μm diameter central W-Re(3%) wire. Electron clusters released from a particle track induce signals on the anode wire. One of the first clusters arriving on the wire triggers the readout electronics. From the known space–drift–time relation, the track distance of the charged particle from the wire is extracted.

The ATLAS muon spectrometer, based on Monitored Drift Tube (MDT) chambers, covers 5500 m^2 and has to provide a stand-alone sagitta measurement. The muons with a momenta up to a few TeV/c have to be measured with a relative precision better than 10% and in the order of 2–3% for muons at around 100 GeV/c.

The single-tube resolution is typically 80 μm. In order to achieve the required sagitta resolution of ~50 μm for the highest muon momenta, each MDT chamber consists of two multilayer of 3–4 mono-layers each of which are glued on either side of a support structure (Fig. 7). Chambers (1200) containing about 400 000 drift tubes of 1–6 m length have been built at 13 construction sites worldwide over a period of 4 years.

To create enough electron–ion clusters in the Ar/CO_2 93/7% gas mixture, the drift tubes have to be operated with a pressure of 3 bar absolute. The

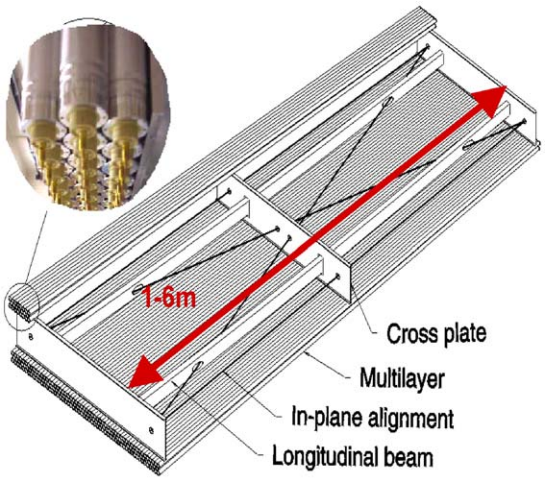

Fig. 7. Schematic of the ATLAS MDT chamber.

gas overpressure reduces the diffusion and improves the chamber resolution, due to higher ionization statistics. To minimize the risk of aging, the gas gain must be set to its lowest possible value. Still, the needed gas gain is $\sim 2 \times 10^4$, which translates over 10 years of operation with a luminosity of $10^{34}\,cm^{-2}s^{-2}$ and a rate of 500 Hz/cm to 1 C/cm [25].

To achieve the physics requirements, various challenging criteria must be fulfilled. The mechanical assembly of the single chamber must be known with respect of a reference system with an accuracy of 20 μm [26]. This is ensured by a precise assembly procedure at the X-ray tomograph facility at CERN [27]. The relation between the measured drift time and the corresponding drift radius has to be determinate with a precision of 20 μm. An internal optical alignment system placed on the spacers structure has to monitor the displacement of the chambers due to the temperature variations and gradients with a relative accuracy of 30 μm [28].

Successful performance tests of large-scale proto-types have been carried out; all required design accuracies have been verified [29].

3. Micro-pattern gaseous detectors

In the preparation for high-luminosity collider experiments, at the LHC, it was understood that

the performance of standard wire chambers, used as central tracking detectors were not sufficient in terms of spatial resolution as well as rate capability. With an amplifying cell size of 1–2 mm (Fig. 8) spatial resolution up to 50 μm and maximal rate capability of 10 kHz/mm^2 can be achieved [30].

In the 80s, advanced etching technology allowed the realization of the Micro Strip Gas Chamber (MSGC) [31]. The MSGC is a position-sensitive proportional counter on a substrate with similar operation principle to that of the MWPC [3]. It consists of thin parallel metal strips, alternatively connected as anodes and cathodes, deposited usually on high-resistive glass plate. Significantly reduced amplifying cells, in the order of ~200 μm (Fig. 8), were built with photolithographic techniques. This detector offered advantages in terms of rate and multi-track capability. Localization accuracy in the order of 30–40 μm and a rate capability exceeding 10^5 Hz/mm^2 have been achieved. Nevertheless, the tiny structure of alternating electrodes creating high-field regions makes this device vulnerable for destruction at the appearance of discharges, when operated at high gains. These breakdowns are enhanced by the exposure to high rate and heavily ionizing particles, and also with the presence of high electric fields on cathode edges due to field emission. To reach safe operating condition, intense effort was made to optimize the substrates, their geometries and operating gases [32,33]. Nevertheless, MSGC were abandoned for the LHC experiments. However, the advanced etching technologies have been used to invent many other position-sensitive microstructure devices working in the proportional amplification mode. These devices, like the micro-CAT [34], GEM [4], MICROMEGAS [5], WELL [35], micro-Groove [36], micro DOT [37] as well as the MSGC and others are known as Micro Pattern Gas Detectors (MPGD).

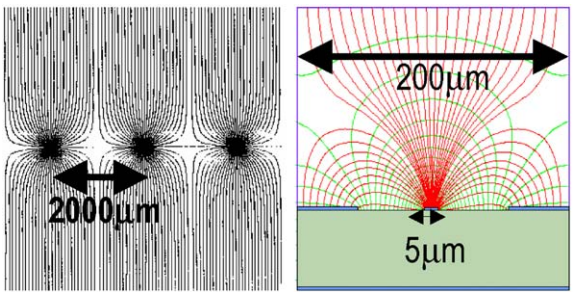

Fig. 8. Electrical field map and cell size of MWPC and MSGC.

A common characteristic of all MPGDs is that high electric field extends over their entire amplification gap between anode and cathode. Different from the amplification on a wire, where the electrical field degrades with $1/r$, a streamer is not anymore self-quenched. Thus a streamer can reach more easily the other electrode and produce a spark [38].

Two representatives of the MPGD, the MICROMEGAS and the GEM detector, are widely investigated by many groups and are successfully operating in high-energy physics experiments. The performance of these two detectors in context and related to the high-energy physics will be discussed. However, MPGD detectors are also widely used in applications beyond high-energy physics.

3.1. MICROMEGAS

The MICROMEGAS detector [5], schematically shown in Fig. 9, is a parallel plate avalanche gas chamber with a single amplification stage operated at atmospheric pressure. It consists of a conversion gap and a narrow amplification region, which is situated between a cathode mesh and the anode readout structure underneath.

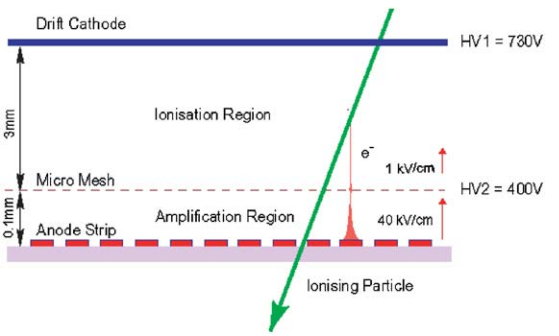

Fig. 9. Schematic of the MICROMEGAS chamber used in COMPASS.

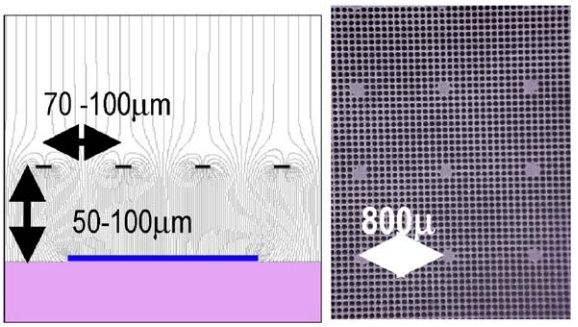

Fig. 10. Electrical field map of a MICROMEGAS amplification cell and a microscope photo of the micromesh.

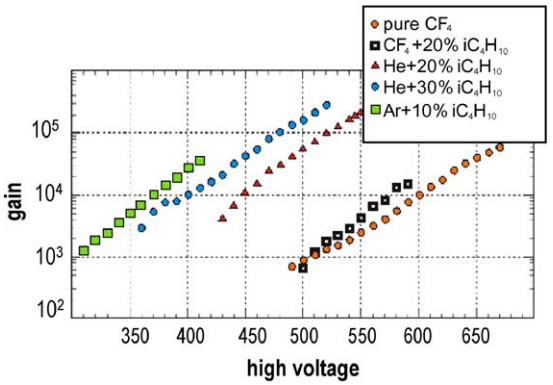

Fig. 11. Gain vs. HV on the micromesh for different gas mixtures.

The width of the conversion gap is, depending on the gas choice, some 2–5 mm, the amplification gap has a size of 50–100 μm. The cathode mesh is made of a thin metallic micromesh (Fig. 10) with a hole-pitch of some 10 μm. The anode readout structure is a simple Printed Circuit Board (PCB) with either strip or pad structure. The high voltage applied on the drift electrode and the wire mesh, forms an electrical field, shown in Fig. 10. Electrons liberated in the conversion gap, by an ionizing particle, follow the electric field lines towards the micromesh and are multiplied in the high field (30–80 kV/cm) of the amplification gap.

Due to the electric field configuration most of the ions produced during the avalanche process are collected rapidly at the cathode micro-mesh, thus when the space charge is kept smaller the detector has a high rate capability. Since the ions drift over the maximum distance of ~50–100 μm, the width of the signal induced on the readout structure is short.

The cathode–anode distance (micromesh-readout structure) is kept constant by small insulating pillars with a pitch of ~1 mm. These pillars, realized by standard photolithographic technique, allow to obtain a uniform electric field in the amplification gap. However, the field configuration in the amplification gap of the detector exploits the saturating characteristics of the Townsend coefficient. This effect reduces the dependence of gain and gap variations. High gains with different gas mixtures have been demonstrated [39] and are shown in Fig. 11.

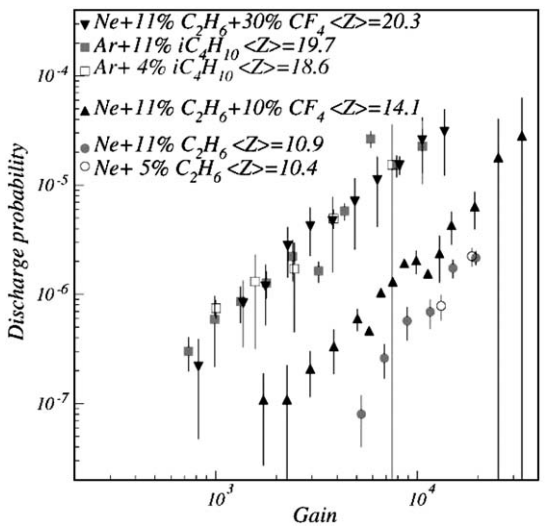

Fig. 12. Discharge probability vs. HV on the micro-mesh for different gas mixtures.

A systematic study of spatial resolution down to 14 μm with different gas mixtures is reported in [40]. At this conference it was reported that the KABES detector integrated in the NA 48 experiment reached a time resolution of 0.6 ns [41].

To minimize the occurrence of discharges, systematic studies with different gas mixtures have been made [42]. The discharge probability versus gain Fig. 12, shows that the probability depends strongly on the mean atomic number $<Z>$ of the used gas mixture.

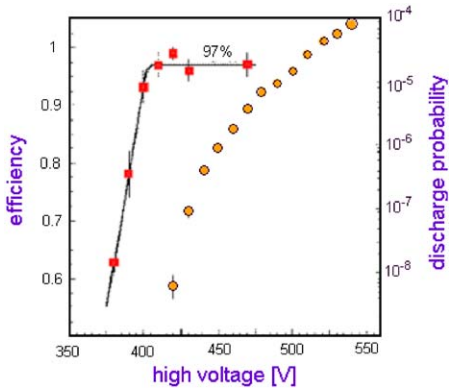

Fig. 13. Detector efficiency and discharge probability vs. HV applied on the micro-mesh.

In spite of the increasing discharge probability at higher amplification, the detector can be operated at full efficiency with relatively low discharge probability, as shown in Fig. 13. Further discharge studies with MICROMEGAS can found in Ref. [43].

3.2. The Gas Electron Multiplier

The Gas Electron Multiplier [4] consists of a 50 μm thick Kapton foil metallized on both sides and perforated by a matrix of ~70 μm diameter holes, with a pitch of about 140 μm. With an applied voltage between the two electrodes, a strong dipole field develops in these holes, where electron amplification takes place. In Fig. 14, a typical field map of the GEM amplification area is shown. An external drift field guides the electrons, released by gas ionization in the conversion gap, towards the GEM foil and into the holes, thus into the amplification channels. The electrons are extracted by a field below the GEM foil and transferred to another amplification foil or to a charge collecting electrode.

A standard GEM chamber consists of a conversion gap, one or several transfer gaps, and an induction gap and below a readout structure, as shown in Fig. 15.

Different field settings of drift-, amplification-, and extraction field result in different charge sharing on the involved electrodes. It is relatively

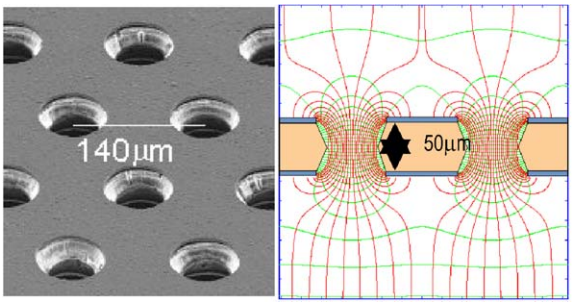

Fig. 14. Electrical field map of a GEM amplification cell and a microscopic photo of the foil.

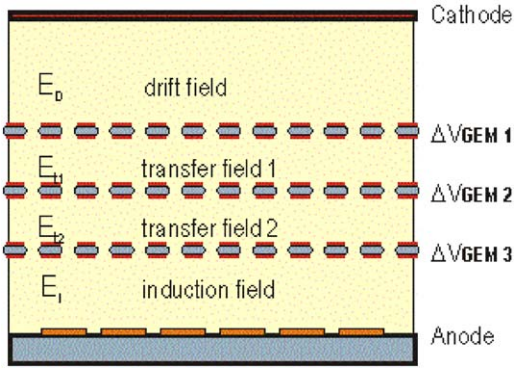

Fig. 15. Schematic view of a triple GEM detector.

easy to tune the field so that almost all primary electrons get guided into the GEM holes. Inside the amplification channel, charges are displaced by diffusion and get trapped on the GEM electrodes. This mechanism reduces the detectable charge on the readout structure, compared to the one produced in the GEM holes. But also a big fraction of the ions, released in the multiplication process, gets absorbed at the GEM electrodes. This effect is called 'ion-feedback', or 'ion-back-flow' suppression. Studies of the charge sharing mechanism in GEM structures as a function of applied fields can be found at [44–48]. Already with a single GEM foil, gains can be reached, which are suitable for direct detection of ionization on simple pickup electrodes [49]. But discharges start to occur at higher gains (above several thousands). The exposure to heavily ionizing

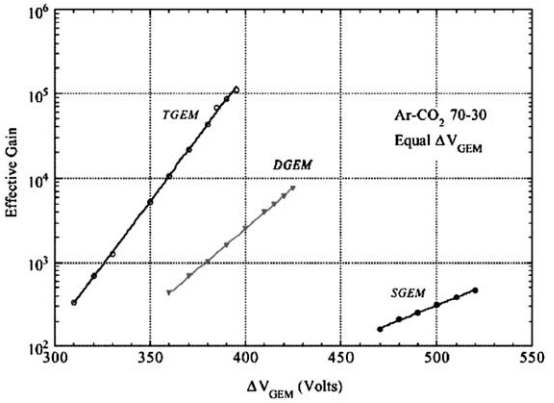

Fig. 16. Gain vs. HV on the GEM-foils for a single, double and triple GEM detector.

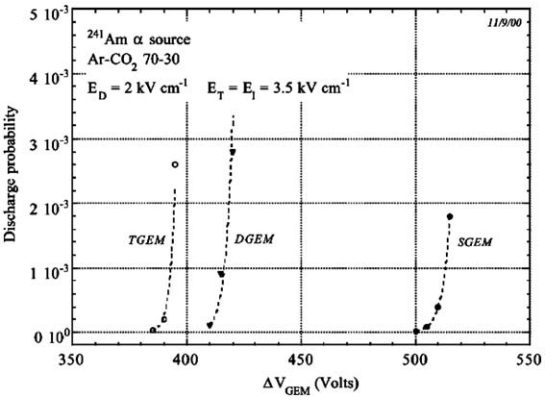

Fig. 17. Discharge probability on α particles vs. high voltage applied on each GEM foil for a single, double and triple GEM structure.

particles reduces the gain limit even to some hundreds.

However, GEM foils can be multi-staged allowing to distribute the amplification over several foils and achieving safe detector operation.

Fig. 16 shows the gain dependence on voltage applied on each GEM foil for a single, double and triple GEM detector [50].

Detailed studies have been performed to minimize discharges occurring in multi-GEM structures [50]. Tests were performed with heavily ionizing α particles, emitted from an ^{241}Am source, positioned close to the GEM amplification channel. The probability of discharges, in the presence of α particles as a function of the effective gain is shown in Fig. 17 for single, double and triple GEM detectors. The authors demonstrate the reduction of discharges, with the use of a multi-stage-amplification structure.

In the COMPASS [51] experiment at CERN, a 'small-area tracking detector' ensemble, based on GEM detectors, is installed. Each of the chambers covers an area of $31 \times 31\,\mathrm{cm}^2$ [52]. For these detectors a 2D readout structure with orthogonal strips has been developed. To realize this structure, the same production techniques have been used as for the fabrication of the GEM foils. The strip readout, with 400 μm pitch for both coordinates, is optimized to get the same signal on x and y strips (Fig. 18).

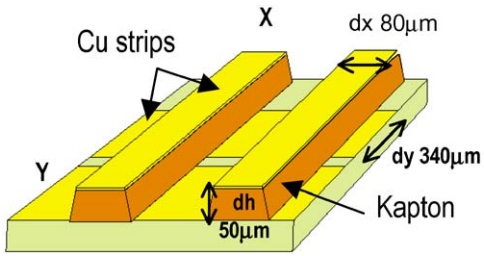

Fig. 18. Schematic of the 2D COMPASS GEM chamber readout.

A spatial resolution of ~50 μm on both coordinates, shown in Fig. 19, could be achieved with these chambers.

The intrinsic high rate capability and the robustness of a multi-GEM structure make this kind of detector interesting for other high-energy physics applications. In the LHCb experiment at CERN, a GEM detector with pad readout will be used in one muon trigger station [53]. With a triple GEM structure, a time resolution of 4.5 ns could be achieved with a $Ar/CO_2/CF_4$ 45–15–40% gas mixture [54].

3.3. Gas photomultiplier with GEM structure

Large area UV-sensitive gaseous detectors, mainly with CsI photocathode coupled to wire

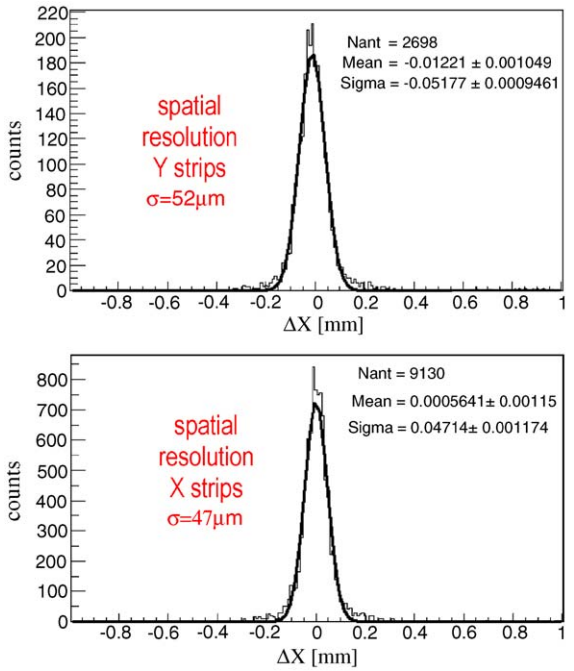

Fig. 19. Spatial resolution difference measured in a 2D COMPASS GEM chamber for x and y coordinates.

chambers, are currently employed in Ring Imaging Cherenkov (RICH) counters [55]. Combining a solid photocathode and a fast GEM gas electron multiplier is an attractive alternative. This combination offers high gains, thus single electron detection is possible. The operation at atmospheric pressure permits the construction of thin and large sensitive areas, high rate capability, <1 ns time resolution and a position resolution $<100\,\mu$m.

The photocathode can be deposited at the uppermost GEM electrode. This so-called ''reflective photocathode'', proposed by Bouclier et al. [56] and realized by Breskin et al. [57], is shown in Fig. 20.

Photoelectrons are emitted from the photocathode and transferred into the first GEM. These electrons are amplified in the following GEM structure and collected on a readout pattern. Due to the opacity of multi-GEM structures, photons created during the avalanche multiplication process, cannot reach the photocathode and thus the photon-feedback is suppressed.

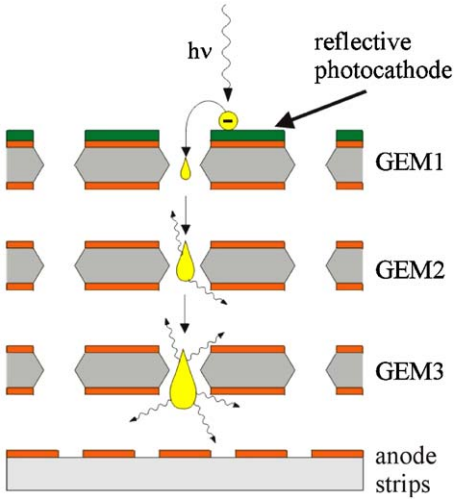

Fig. 20. Schematic of a triple GEM photo-detector with a reflective photocathode deposited on the upper electrode of the GEM foil.

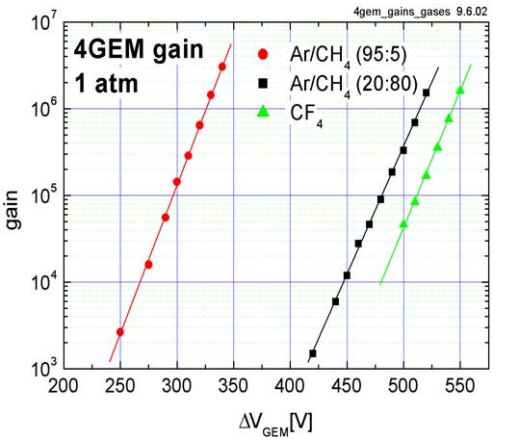

Fig. 21. Gas gain of a gas photomultiplier with a CsI photocathode vs. high voltage on the GEM foils for different gas mixtures.

The intrinsic ion-feedback suppression of the chamber lowers the background induced by the ions and reduces the photocathode degradation, due to ion bombardment [58]. Such a detector assembly can reach high gains of up to 10^6 with different gas mixtures, as shown in Fig. 21. The signal response is very fast, 1.5 ns for single photon detection and 0.3 ns for ~200 photons.

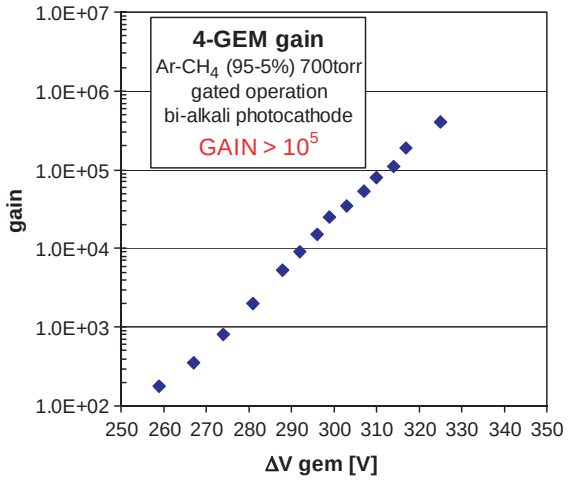

Fig. 22. Gain curve for a gated multi-GEM gas photomultiplier with a bi-alkali photocathode.

Recently, a breakthrough was made in operating for a longer period a gas photomultiplier with a bi-alkali photocathode (K–Cs–Sb) [59,60]. These photocathodes are sensitive to the visible light spectrum (350–700 nm). Since this photocathode can easily be degraded due to impurities, the chamber has to be carefully filled with gas in ultra-clean conditions and sealed. The detector, with a semi-transparent photocathode, was operated in the sealed mode for several weeks. In this mode, high gains and stable quantum efficiency of the photocathode could be achieved with an Ar–CH_4 95–5% gas mixture. To guarantee the quantum efficiencies over a longer period, an additional gating grid blocked all ions escaping the GEM structure. This arrangement allows to reach gains $>10^5$, shown in Fig. 22 [61].

3.4. MPGD for a linear collider experiment

Good localization accuracy, multi-track resolution, and high rate capability make micro-pattern gaseous detectors, like the Gas Electron Multiplier or the MICROMEGAS, a good choice for readout structures in future high performing collider experiments.

Recently, it was agreed that the next large accelerator project after the startup of the LHC should be a high-luminosity electron–positron linear collider, with a central mass energy up to 1 TeV. The LC will have a bunch train frequency of 5 Hz, while the bunch train lasts 1 ms. This time structure has large implications for the overall detector design. A TPC is foreseen for the central tracker of the future TESLA experiment, which will be installed in the e^+e^- linear collider [62].

The physics requirements for such a TPC are very demanding. Over a maximal drift length of 2500 mm a lateral space point resolution ~100–150 μm, a multi-track separation of 2.3 mm ($r-\phi$), 10 mm (z), and 5% dE/dx resolution have to be reached. These requirements are beyond the limits of MWPCs, but might be achieved with MPGD. GEM-type, as well as the MICROMEGAS detectors are currently under intense investigation by several groups [63].

Further features of this type of readout chambers are promising.

Distortions generated by the $\boldsymbol{E}\times\boldsymbol{B}$ effect in wire chamber geometries are largely reduced, since GEM and MIROMEGAS have parallel plate geometry. The signal spread on the readout structure is just some hundred μm. Already for the ALICE TPC, a GEM-based readout was investigated [20,64]. This solution was abandoned, since it would have required a too large number of readout channels. To reduce the number of readout channels for large detector areas, and conserve good special resolution, the use of a readout plate with a resistive layer is under investigation [65]. Another very attractive feature is the intrinsic suppression of positive ion feedback. To avoid field distortions due to the ion drift in the TPC field cage, ions produced in the readout structures are commonly suppressed by an additional wire mesh, the gating grid. Contributions to this conference have demonstrated that both detector types show intrinsic ion feedback suppression factors in the order of 10^{-3} [66,67].

The intrinsic ion feedback suppression in combination with modern low-noise electronics could therefore allow to not install a gating grid. In this way, the time structure of the e^+e^- linear collider could be handled.

Fig. 23 shows the ion feedback of a MICROMEGAS detector versus the ratio of drift–amplification field. The amount of ions escaping from

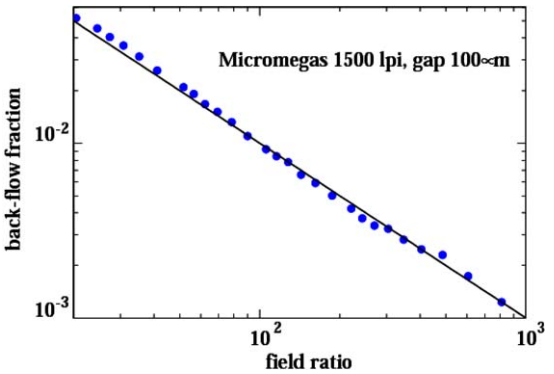

Fig. 23. Ion feedback suppression for a MICROMEGAS chamber with a 1500LPI micro-mesh.

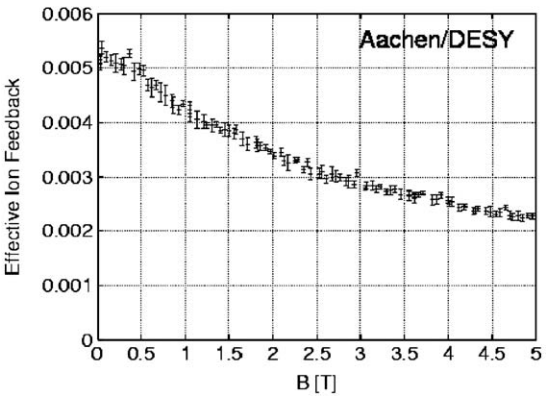

Fig. 24. Ion feedback at constant signal pulse height vs. magnetic field for a multi-GEM structure.

the amplification structure into the drift region can be roughly estimated by the ratio of the drift field to the amplification field. This rough estimation agrees quite well for a single stage amplification structure, like MICROMEGAS with a micromesh pitch of 1500LPI (Lines Per Inch).

For a multistage amplification structure, like GEM, it is slightly different due to the more complex geometry, but the basic principle of ion feedback suppression is roughly the same.

In the frame work for the TESLA TPC, the charge sharing in the presence of a high magnetic field was investigated [68]. Fig. 24 shows the ion backflow into the drift region, at constant pulse height, for increasing parallel magnetic field. This effect is explained by the improved electron extraction of the GEM foils in the presence of magnetic field.

4. Resistive plate chamber

Resistive plate chambers were developed in the 80s [6]. They have been intensively studied by many groups in the last years, in order to meet the challenge of the LHC. The goal is to produce an affordable large-area detector with good timing ($\sim$1 ns), space resolution, and sufficient rate capability ($<1\,\mathrm{kHz/cm^2}$) for trigger purposes. The standard Trigger RPC has 2 mm gas gap and resistive electrodes made out of phenolic–melaminic. Further developments opened the possibility to use this kind of detector for a high resolution Time-of-Flight system. The so-called, Multigap RPC [69] or Timing-RPC [70] have multi-stacked gas gaps of 200–300 μm and achieve a timing resolution in the order of 50–100 ps. This performance is comparable to the one of Pestov counters. However, to reach high efficiency with a Pestov counter [71], the operational gas pressure has to be 12 atm, which introduces important mechanical constrains.

These detectors can be operated either in a streamer mode or in an avalanche mode. Chambers operated in streamer mode produce large signals, which are easy to discriminate. Modern electronics allows operating the RPC in avalanche mode. This reduces the charge produced during multiplication, thus better rate capability can be achieved. The avalanche mode operation seems to have advantages on the long-term stability of the chambers in highly irradiated areas also.

RPC detector physics for the Trigger RPC, as well as for narrow gap RPCs have been simulated by several authors [72–74]. With modern simulation tools, a good agreement between simulation and experimental data could be achieved recently. Trigger RPCs operate with a field of $\sim$50 kV/cm in the gas gap, while the operational field for Timing- and Multigap RPCs is above 100 kV/cm. The Townsend coefficient α and the attachment coefficient η for these fields are shown in Fig. 25 [75]. For the trigger RPC an 'effective Townsend coefficient' ($\alpha-\eta$) of $\sim$10/mm may be obtained,

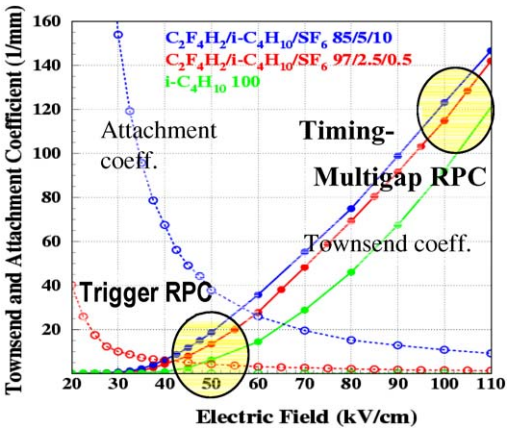

Fig. 25. Townsend (solid line) and attachment (dashed line) coefficient as a function of the electric field for different gases.

while for the narrow gap RPCs it may reach $\alpha_{\text{eff.}} > 100/\text{mm}$.

The different operation condition has large consequences for the mechanism of the avalanche process in the gas gap. The charge multiplication process in RPCs working with high α_{eff}, are dominated by a saturation phenomenon. At high amplifications, the ion cloud will screen the electrical field, and thus stop the avalanche growth.

4.1. Trigger RPC

Fig. 26 shows a schematic of a standard Trigger RPC with 2 mm gas gap, resistive electrodes made out of phenolic–melaminic (Bakalite), and carbon electrodes to apply the high voltage and on either side, insulated from the HV pickup electrodes.

The ATLAS RPC trigger chambers have a total size of $80 \times 320\,\text{cm}^2$ each and have to cover 3600m^2. The RPC signals are picked up by a system of 32 strips orthogonal to each other on both sides of each gas gap. The chambers operate in the avalanche mode and reach detector efficiency of ~97% and a time resolution of ~1.6 ns [76].

4.2. Multigap and high-rate timing RPC

MultigapRPC [69] is a pile of resistive glass plates separated by a 250 μm thin spacer, shown in

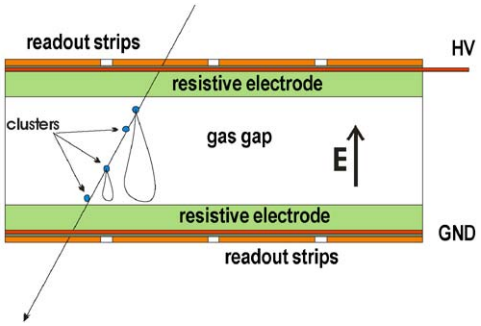

Fig. 26. Schematic of a standard trigger RPC.

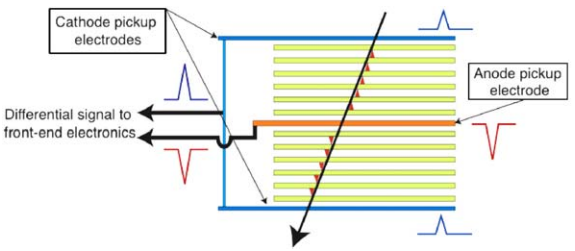

Fig. 27. Schematic of a Multigap RPC.

Fig. 27. High voltage is applied on the external surfaces of the outer electrodes, while the internal plates are electrically floating and get their correct potential by electrostatic equilibrium. A particle traversing the chamber creates in the small gaps several avalanches simultaneously.

These avalanches induce a signal in the pickup electrodes (strips or pads) on both sides of the chamber, as well as on the middle one. The signal induced on the electrodes is the sum contribution of all gaps. Consequently, with such an assembly, high efficiencies can be achieved. Time resolution depends on the drift distance of the single gap. Since the gaps are small, the time resolution in the order of 50 ps can be achieved. The width of the gas gaps has to be chosen in combination with the desired gas to be large enough so that enough clusters are produced. This technology has been chosen for the ALICE TOF detector. The chamber consists of two stacks of five gaps, thus a unit has 10 gaps of 250 mm. Gas gap spacing is ensured by nylon fishing lines.

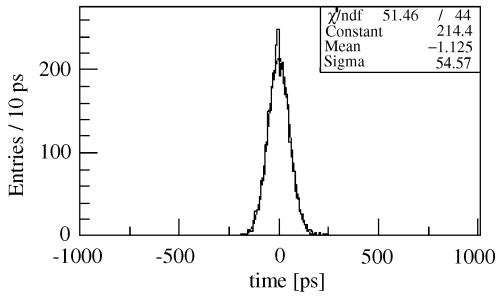

Fig. 28. Time distribution of the ALICE TOF Multigap RPC.

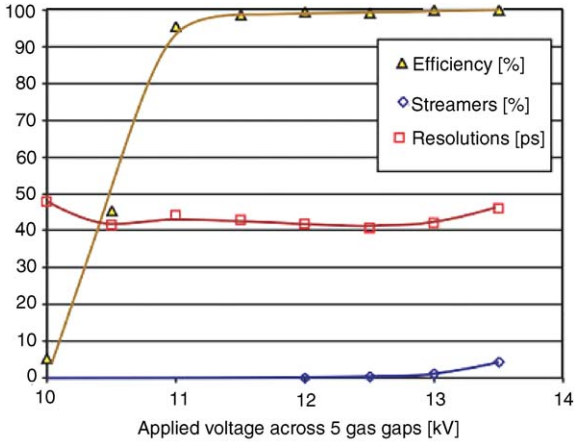

Fig. 29. Efficiency and time resolution vs. applied high voltage across a 5-gap MRPC.

A typical time distribution of the ALICE TOF MRPC is shown in Fig. 28 [77]. The time resolution of 55 ps has been corrected for slewing. Fig. 29 shows a typical efficiency of 99.9% and the time resolution below 50 ps range vs. the applied field on the MRPC [78].

Recent development of new materials for the resistive plates has enabled High rate Timing RPCs to reach rate capabilities up to 25 kH/cm^2 [79].

5. Summary and outlook

Gaseous detectors, in particular wire chambers, have been an indispensable element in HEP experiments for the last three decades. Their technology is well known and proven to be robust, precise and reliable. Several large and complex detector ensembles, being assembled right now, demonstrate that standard wire chamber technology is still up to date and very effective. Modern simulation tools are available for efficient gas detector development and novel gas mixtures allow safe detector operation.

In the past years, micro-pattern gaseous detectors have proven to be reliable and permit fast signal response and good spatial resolution combined with high rate capability. Their promising features and capabilities motivated their proposal for future projects with stringent requirements as for a new linear collider. Advanced electronics enlarged the range of applications for gaseous detectors in general. For RPCs, this advancement permitted to operate the chambers in the avalanche mode. The RPC technology advanced from a trigger counter to a highly efficient and fast time of flight detector with high rate capability.

After all these years of highly successful implementation in high-energy experiments, various contributions to the VCI 2004 exhibit that gaseous detector development continues to be very active. Further improvements are needed to meet the challenges of future projects, which guarantee an exciting future.

References

[1] H. Geiger, E. Rutherford, Proc. Roy. Soc. A 81 (1908) 141.
[2] H. Geiger, W. Müeller, Phy. Zeits. 29 (1928) 839.
[3] G. Charpak, et al., Nucl. Instr. and Meth. 62 (1968) 262.
[4] F. Sauli, Nucl. Instr. and Meth. A 368 (1997) 531.
[5] Y. Giomataris, et al., Nucl. Instr. and Meth. A 376 (1996) 29.
[6] R. Santonico, R. Cadarelli, Nucl. Instr. and Meth. 187 (1981) 377.
[7] Ansoft Co, Maxwell Pittsburg, PA ,USA.
[8] I. Smirnov, Heed CERN, 1996.
[9] S. Biagi, Magboltz Liverpool University, UK, 1997.
[10] R. Veenhof, Nucl. Instr. and Meth. A 419 (1998) 726.
[11] MATEMATICA, Wolfram Research, Inc., 2003.
[12] B. Schnitzer, et al., Simple models for RPC weighting fields and potentials, Proceedings of VCI, 2004.
[13] PSPICE, Cadence Design System, Inc. US, 2003.
[14] D.R. Nygren, et al., Proposal PEP No 4, Appendix A 6.
[15] H.J. Hilke, et al., Nucl. Instr. and Meth. 161 (1979) 383.

[16] K.H. Ackermann, et al., Nucl. Instr. and Meth. A 499 (2003) 624.
[17] E.O'Brien, et al., Experimental overview at RHIC, Nucl. Instr. and Meth. A, (2004) these Proceedings.
[18] M. Anderson, et al., Nucl. Instr. and Meth. A 499 (2003) 659.
[19] ALICE Technical proposal for a large ion collider experiment at the CERN LHC, CERN/LHCC/95-71, 1995.
[20] ALICE TPC, CERN/LHCC 2000-001 Alice TDR 7, 2000.
[21] R. Veenhof, Choosing a gas mixture for the ALICE TPC, ALICE-INT-2003-29.
[22] A. Afanasiev, et al., Nucl. Instr. and Meth. A 430 (1999) 210.
[23] ATLAS muon spectrometer, CERN/LHCC/97-22, ATLAS TRD 10, 1997.
[24] CMS muon project, CERN/LHCC/97-32, CMS TRD 3, 1997.
[25] C. Cernoch, et al., Recent and ongoing ageing studies for the ATLAS muon spectrometer drift tubes, Proceedings of VCI, 2004.
[26] C. Bacci, et al., ATL-MUON-97-135; ATL-M-PM 135.
[27] S. Schuh, et al., Nucl. Instr. and Meth. A 518 (2004) 73.
[28] C. Amelung, A. Schricker, ATLAS muon note July 12, 2002.
[29] F. Cerutti, et al., Performance studies of the MDT chambers of the ATLAS muon spectrometer, Nucl. Instr. and Meth. A, (2004) these Proceedings.
[30] L. Shekhtman, Nucl. Instr. and Meth. A 494 (2002) 128.
[31] A. Oed, Nucl. Instr. and Meth. A 263 (1988) 351.
[32] F. Angelini, et al., Nucl. Instr. and Meth. A 283 (1989) 755.
[33] R. Bouclier, et al., Nucl. Instr. and Meth. A 323 (1992) 240.
[34] A. Sarvestani, et al., Nucl. Instr. and Meth. A 454 (1998) 238.
[35] R. Bellazzini, et al., Nucl. Instr. and Meth. A 424 (1999) 444.
[36] R. Bellazzini, et al., Nucl. Instr. and Meth. A 423 (1999) 125.
[37] S.F. Biagi, et al., Nucl. Instr. and Meth. A 361 (1995) 72.
[38] A. Bressan, et al., Nucl. Instr. and Meth. A 424 (1999) 321.
[39] A. Delbart, et al., Nucl. Instr. and Meth. A 461 (2001) 84.
[40] J. Derre, et al., Nucl. Instr. and Meth. A 477 (2002) 23.
[41] B. Peyaud, et al., KABES-anew detector for high intensity beams, Nucl. Instr. and Meth. A, (2004) these Proceedings.
[42] D. Thers, et al., Nucl. Instr. and Meth. A 469 (2001) 133.
[43] A. Bay, et al., Nucl. Instr. and Meth. A 488 (2002) 162.
[44] S. Bachmann, et al., Nucl. Instr. and Meth. A 438 (1999) 376.
[45] A. Breskin, et al., Nucl. Instr. and Meth. A 478 (2002) 538.
[46] A. Bondar, et al., Nucl. Instr. and Meth. A 496 (2003) 325.
[47] D. Mormann, et al., Nucl. Instr. and Meth. A 516 (2004) 315.
[48] M. Hoch, Development of fast tracking detectors: MSGC and GEM Thesis Vienna/CERN, 1998.
[49] J. Benelloch, et al., IEEE Trans. Nucl. Sci. NS-45 (1998) 234.
[50] S. Bachmann, et al., Nucl. Instr. and Meth. A 479 (2002) 294.
[51] G. Baum, et al., COMPASS proposal, CERN-SPSLC-96-14, 1996.
[52] B. Ketzer, et al., IEEE 48 (4) (2001) 1065.
[53] C. Altunbas, et al., Nucl. Instr. and Meth. A 490 (2002) 177.
[54] M. Alfonsi, et al., Nucl. Instr. and Meth. A 518 (2004) 106.
[55] F. Piuz, et al., Nucl. Instr. and Meth. A 433 (1999) 222.
[56] R. Bouclier, et al., IEEE Trans. Nucl. Sci. NS-44 (1997) 646.
[57] A. Breskin, et al., Nucl. Instr. and Meth. A 478 (2002) 230.
[58] D. Mörmann, et al., Nucl. Instr. and Meth. A 516 (2004) 315.
[59] D. Mörmann, et al., Nucl. Instr. and Meth. A 504 (2003) 93.
[60] M. Balcerzyk, et al., IEEE Trans. Nucl. Sci. NS-50 (2003) 847.
[61] R. Chekin, et al., Thick GEM-like multipliers: properties and possible applications, Proceedings of VCI, 2004.
[62] TESLA Technical Design Report, Part IV, DESY-01-011, 2001.
[63] J.E. Augustin, Detector concepts for a linear collider, Nucl. Instr. and Meth. A, (2004) these Proceedings, and references there in.
[64] M. Hoch, et al. Proceedings of Workshop on Micro Pattern Gas Detectors, Orsay, 1999.
[65] M.S. Dixit, et al., Nucl. Instr. and Meth. A 518 (2004) 721.
[66] V. Lepetier, et al., Proceedings of IEEE, Portland, 2003.
[67] S. Roth, et al., Charge Transfer of GEM structures in high magnetic fields, Nucl. Instr. and Meth. A, (2004) these Proceedings.
[68] S. Roth, et al., Proceedings of ICCTP, Como, 2003.
[69] Cerron, et al., Nucl. Instr. and Meth. A 374 (1996) 132.
[70] P. Fonte, et al., Nucl. Instr. and Meth. A 443 (2000) 201.
[71] V. Pestov, et al., Nucl. Instr. and Meth. 93 (1971) 269.
[72] M. Abbrescia, et al., Nucl. Instr. and Meth. A 398 (1997) 173.
[73] P. Fonte, Nucl. Instr. and Meth. A 456 (2000) 6.
[74] W. Riegler, et al., Nucl. Instr. and Meth. A 500 (2003) 144.
[75] W. Riegler, et al., Nucl. Instr. and Meth. A 508 (2003) 14.
[76] A. Di Mattia, et al., Nucl. Instr. and Meth. A 518 (2004) 529.
[77] D. Hatzifotiadou, Nucl. Instr. and Meth. A 502 (2003) 123.
[78] D. Hatzifotiadou, et al., Proceedings of RPC workshop, France, 2003.
[79] P. Fonte, et al., Progress in timing resistive plate chambers, Proceedings of VCI, 2004.